INVESTIGATION ON ENHANCING THERMAL PERFORMANCE OF THE LI-ION BATTERY PACK WITH FISHBONE CHANNEL LIQUID COOLING PLATE AND OPTIMIZED FLOW CHANNELS

LingYun ZHANG, XiaoQin LIU*,Li GAO,JianYong WANG*

School of Mechanical and Electrical Engineering, Shaanxi University of Science and Technology, Xian, China

*Corresponding author; E-mail: xiaoqinliu@sust.edu.cn, jywang@sust.edu.cn

Effective thermal management is essential for ensuring the safety and high performance of electric vehicle battery packs. This paper investigates the optimization of a fishbone flow channel structure through three strategies: a tapered main channel, reduced rear branch width, and the addition of branch flow channels. Numerical results from ANSYS Fluent indicate that compared to the baseline fishbone channel, a tapered design with a 2 mm outlet width reduces the maximum temperature to 37.21 °C, a 0.12 °C decrease, and lowers the temperature standard deviation by 0.04 °C to 0.51 °C. However, a 12% pressure drop increase offsets the 7% gain in the heat taken away by the coolant, limiting the improvement in the comprehensive performance evaluation factor to only 0.7%.Reducing the rear branch width to 2 mm constrains the temperature standard deviation to 0.50 °C, which is 0.05 °C lower than the original channel, with minimal impact on other metrics. Expanding branch channels is the most effective strategy for heat transfer enhancement. Specifically, a structure with a 6 mm branch length reduces the maximum temperature by 0.54 °C to 36.79 °C and decreases the temperature standard deviation to 0.52 °C.Furthermore, this configuration achieves an 18% reduction in pressure drop, while the heat taken away by the coolant and the comprehensive performance evaluation factor increase by 3% and 15%, respectively. These findings provide a quantitative basis for designing high-efficiency liquid cooling plates.

Key words*: battery thermal management system, a tapered main channel, reduced rear branch width, added branch flow channels, numerical simulation*

1. Introduction

Currently, there are four primary cooling methods for BTMS: air cooling , liquid cooling, and phase change material (PCM) cooling[1,2]. Liquid cooling technology has received widespread attention due to its high heat transfer efficiency [3], low cost, and excellent stability. Most research on liquid cooling systems focuses on optimizing the cold plates and cooling channels. Qi et al. [4] designed a multi-U-shaped microchannel cold plate, which showed better overall and heat transfer performance than traditional series and parallel channels. Fan et al. [5] added unidirectional secondary channels and

grids to a traditional serpentine channel. Although this increased the battery temperature, it drastically reduced pump power consumption by 92.6%, and the cooling efficiency coefficient jumped by a factor of 12.32. Aldawi [6] found that wavy channels outperformed straight and zigzag channels in both parallel and counter-flow setups. Wu et al. Wu et al. [7] found that cylindrical channels provided better heat dissipation than straight, elliptical, and prismatic channels. Gan et al. [8] proposed a symmetrical double-helical channel that prevented localized hotspots by creating a uniform flow field and alternating hot and cold fluid streams. Through the clever design of fins within liquid cold plate channels, convective heat transfer performance can be significantly improved, a method that many scholars have studied. Xie et al. [9] added separators to the flow channel to intensify coolant turbulence. Their cold plate, with 20 double-sided separators, effectively reduced the maximum temperature and temperature difference but inevitably increased system energy consumption. Zhu et al. [10] proposed a cold plate with alternately staggered ribs and grooves that lowered the battery pack temperature with only a slight increase in pressure drop. Zhang et al. [11] introduced six new letter-shaped fins, finding that the novel letter-shaped fins exhibit a superior field synergy effect, effectively minimizing heat transfer's irreversibility. Ahmed et al. [12] optimized the geometric parameters of a grooved microchannel, achieving a significant 51.59% enhancement in heat transfer performance at a Reynolds number of 100 while increasing the friction coefficient by only 2.35%. Mohapatra et al. [13] investigated the improved mini-channel cold plate and fragmented design. The modified design enhances heat transfer performance while reducing pressure drop.

The effectiveness of a liquid cooling system for battery thermal management depends heavily on the design of its flow channels and the thermal-flow properties of the coolant. The fishbone flow channel, inspired by nature, uses its distinctive branching structure to optimize flow resistance and heat transfer. This approach significantly reduces system pressure drop and the maximum temperature difference, improving temperature uniformity and energy efficiency. However, a major limitation of traditional fishbone channels is their tendency to create a noticeable temperature gradient, especially downstream, where lower flow velocity greatly decreases heat transfer. To address this, this paper proposes several optimization strategies based on the basic fishbone design. We aim to enhance overall temperature uniformity and lower the maximum battery temperature by introducing a tapered main channel, reducing the width of downstream branches, and adding the number of branch flow channels. This study will systematically evaluate key parameters such as the maximum battery pack temperature and temperature standard deviation, as well as the cold plate's pressure drop, heat transfer rate, and performance evaluation criterion, to comprehensively analyze the cooling performance of the optimized design.

2. Model and Methods

2.1. Physical Model

The battery pack used in this study was assembled using commercial prismatic lithium-ion batteries(LIBs), each with a nominal capacity of 45 Ah, a nominal voltage of 3.2 V, and dimensions of 200 mm × 150 mm × 30 mm. The electrode materials consist of a lithium iron phosphate ($LiFePO_4$) cathode and a graphite anode. The electrolyte used is 1 M LiPF6–PC/EC/EMC (1/3/5 in weight ratio). The BTMS was simplified to simplify finite element simulations by excluding internal electrodes, localized heat generation at the battery tabs, and some electrical and mechanical auxiliary parts to prioritize macro-level thermal behavior and improve computational efficiency.2 mm thick thermal pads were used to reduce contact thermal resistance between batteries. The aluminum liquid cold plate

featured a single-inlet, dual-outlet fishbone flow channel design, following the method described in Reference [14]. Its overall size was 402 mm long, 158 mm wide, and 4 mm thick. All internal channels were rectangular: the main central channel and the two converging channels on either side measured 12 mm wide, while the 24 dendritic branches were each 4 mm wide. The liquid cooling channels were consistently 2 mm thick, as shown in Fig. 1. A 40% ethylene glycol aqueous solution was used as the coolant inside the cold plate.

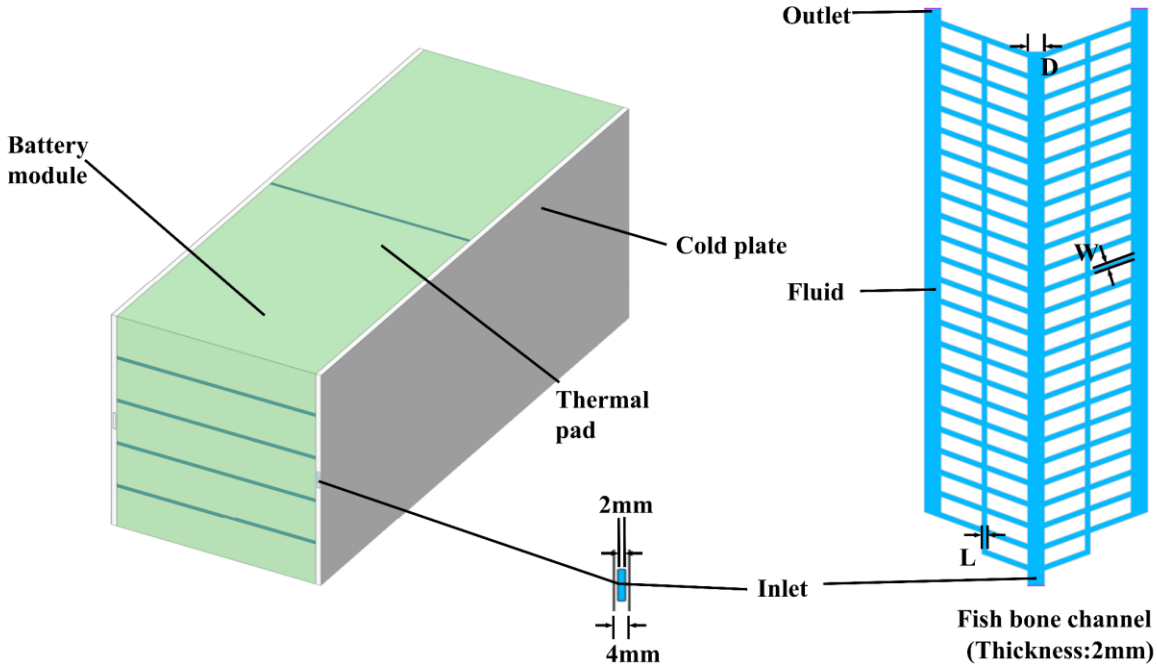

Fig.1. Schematic diagram of the battery pack and liquid cooling plate

2.2. Mathematical Model

2.2.1 Governing equations

The flow in the liquid-cooled plate is an incompressible transient flow. The continuity, momentum, and energy equations[15] in the fluid domain are represented by Eq. (1), Eq. (2), and Eq. (3), respectively, where the influence of gravity is neglected. The specific forms are as follows:

$$\frac{\partial \rho_c}{\partial t} + \nabla \cdot \left(\rho \cdot \vec{v} \right) = 0 \tag{1}$$

$$\frac{\partial}{\partial t}\left(\rho \vec{v} \right) + \nabla \cdot \left(\rho \vec{v} \cdot \vec{v} \right) = -\nabla P + \mu \nabla^2 \vec{v} \tag{2}$$

$$\frac{\partial}{\partial t}\left(\rho C_p T \right) + \nabla \cdot \left(\rho C_p \vec{v} T \right) = \nabla \cdot \left(\lambda \nabla T \right) \tag{3}$$

Where ρ ($\mathrm{J \cdot K^{-1}}$) is the density; c_p ($\mathrm{J \cdot kg^{-1} \cdot K^{-1}}$) is the specific heat capacity; $\vec{v}$ ($\mathrm{m \cdot s^{-1}}$) is the velocity vector; T (K) is the temperature; P (Pa) is the hydrostatic pressure, the unit is Pa; μ ($\mathrm{N \cdot s \cdot m^{-2}}$) is the dynamic viscosity; λ ($\mathrm{W \cdot m^{-1} \cdot K^{-1}}$) is the thermal conductivity.

The Reynolds number was calculated using the formula in Eq. (4).

$$Re = \frac{\rho v_{\mathrm{in}} d_e}{\mu} \tag{4}$$

Where d_e (m)is the hydraulic diameter, and v_{in} ($\mathrm{m \cdot s^{-1}}$)is the inlet velocity.

Based on a critical Reynolds number of 2300[16], when the mass flow rate exceeds this threshold, the flow transitions from laminar to turbulent. After calculation, when the mass flow rate is 0.04 kg/s, Re = 2532. The standard $\kappa-\varepsilon$ turbulence model has been widely used in numerical simulations of battery liquid cooling [17,18]. The standard $\kappa-\varepsilon$ turbulence model was chosen. The governing equations for turbulent kinetic energy (κ) and turbulent dissipation rate (ε) [14]in the model are given by Eqs. (5) and (6), respectively.

$$\frac{\partial(\rho k)}{\partial t}+\frac{\partial(\rho k u i)}{\partial x i}=\frac{\partial}{\partial}\left[\left(\mu+\frac{\mu_t}{x j}\right)\frac{\partial k}{\partial x j}\right]+G_k-\rho\varepsilon \tag{5}$$

$$\frac{\partial(\varepsilon)}{\partial t}+\frac{\partial(\rho\varepsilon u i)}{\partial x i}=\frac{\partial}{\partial x j}\left[\left(\mu+\frac{\mu_t}{\sigma\varepsilon}\right)\frac{\partial\varepsilon}{\partial x j}\right]+G_{1\varepsilon}G_k-C_{2\varepsilon}\rho\frac{\varepsilon^2}{k} \tag{6}$$

where G_k represents the turbulent kinetic energy caused by the mean velocity gradient. $C_{1\varepsilon}$ and $C_{2\varepsilon}$ are constants ($C_{1\varepsilon}$ =1.44, $C_{2\varepsilon}$ =1.92, C_μ =0.09, σ_k and σ_ε are the turbulent Prandtl numbers for κ and ε , respectively (σ_k =1.0, σ_ε =1.3).

A constant heat generation rate is assumed to simplify the battery pack's cooling design. The battery is presumed to have a steady and uniform internal heat source, and thermal radiation is neglected. The temperature distribution of a single cell can be solved by the energy Eq. (7)[19]:

$$\rho_b C_{p,b}\frac{\partial T}{\partial t}=\nabla\left(\lambda_b\nabla T\right)+Q_{gen} \tag{7}$$

Where is Q_{gen} the heat generated during the battery charging and discharging process, ρ_b ($J\cdot K^{-1}$) is the battery density, $c_{p,\ b}$ ($J\cdot kg^{-1}\cdot K^{-1}$) is the battery specific heat capacity, and λ_b ($W\cdot m^{-1}\cdot K^{-1}$) is the thermal conductivity of the battery.

The heat generated during battery charging and discharging is related to parameters such as current, voltage, and battery state of charge (SOC). In this study, the discharge intensity is expressed by the C-rate (C), which is defined as the measurement of the charge or discharge current normalized against the battery's nominal capacity (e.g., a 1C rate dispatches the full rated capacity in one hour). Using multiple experimental data, Li [20] fitted the experimental correlation between heat generation and discharge time, given by Eq. (8). The polynomial coefficients are shown in Tab .1.

$$Q_{\text{gen}}=A_1t6+A_2t5+A_3t4+A_4t3+A_5t2+A_6t+A_7 \tag{8}$$

Table 1

Polynomial coefficients of heat generation during the battery discharging process

Discharge rates	A_1	A_2	A_3	A_4	A_5	A_6	A_7
1C	4.9132×10^{16}	-3.7742×10^{12}	1.0679×10^{8}	-1.3417×10^{5}	0.0076	-2.2208	17151.7482
2C	1.2578×10^{-13}	-4.8310×10^{-10}	6.8347×10^{-7}	-4.2934×10^{-4}	0.1216	-17.763	66623.3365

2.3. Boundary conditions

The numerical model was developed and solved using the finite volume method within the ANSYS Fluent environment. The battery pack was simulated at a constant 2C discharge rate, with each cell treated as a uniform heat source. For the thermal environment, the ambient temperature was set to 25 °C, and natural convection was applied to the outer surfaces of the battery and the cold plate with a heat transfer coefficient of 5 $W\cdot m^{-2}\cdot K^{-1}$, while thermal radiation was neglected. Regarding the fluid domain, the coolant inlet was defined as a mass flow inlet with a constant rate of 0.04 kg/s at 25 °C, and

the outlet was set as a pressure outlet with a gauge pressure of 0 kPa. To resolve the near-wall flow, Standard Wall Functions were employed, and the Viscous Heating option was enabled to account for the thermal effects of fluid friction within the narrow channels. The interface between the fluid and solid domains was configured as a no-slip wall with coupled thermal conditions to ensure accurate heat transfer. Detailed material properties used in the simulation are provided in Tab. 2.

Table 2

Material properties used in the simulation.

parameters	40% Ethanol Solution	Aluminum	Battery [21]	Thermal pad
Density ρ ($kg \cdot m^{-3}$)	1055.39	2719	2090	2000
Heat capacity c_p ($j \cdot K^{-1} \cdot kg^{-1}$)	3502	872	1014.4	1270
Thermal conductivity λ ($W \cdot m^{-1} \cdot k^{-1}$)	0.412	202.4	$\lambda_x=\lambda_z=29.94$ $\lambda_z=1.696$	2
Dynamic viscosity μ ($kg \cdot m^{-1} \cdot s^{-1}$)	0.00226			
Nominal Capacity (Ah)			45	
Nominal Voltage (V)			3.2	
Charge Cut-off Voltage (V)			3.6	
Discharge Cut-off Voltage (V)			2.5	
Maximum charging current (A)			≤3	
Maximum discharge current (A)			≤4	
Internal resistance (mΩ)			≤10	

2.4. Performance Indicators

This study uses multiple performance indicators to describe the performance of the power battery thermal management system. The maximum temperature $T_{\max}$ (°C) of the battery and the standard temperature deviation T_{σ} (°C) are used to measure the temperature distribution characteristics of the battery pack. The lower these two values, the more effective the cooling capacity of the liquid-cooled plate is. The definition of T_{σ} is given by Eq. (9):

$$T_{\sigma} = \sqrt{\frac{\sum_{1}^{n}\left(T_j - T_{avg}\right)^2}{n}} \tag{9}$$

Where T_{avg} is the average temperature of the battery pack, and T_j is the average temperature of each battery.

The flow pressure loss $\triangle P$ (Pa) of the liquid cold plate and the comprehensive performance evaluation factor (PEC) are important parameters for assessing the thermal performance of the cold plate. PEC is typically expressed as the dimensionless heat transfer coefficient j ratio to the friction coefficient f. The coefficient j represents the dimensionless surface heat transfer capability, while f is the dimensionless surface friction coefficient, reflecting the channel's flow resistance. Their definitions are as follows Eq. (10), Eq. (11), Eq. (12), Eq. (13):

$$\triangle P = P_{in} - P_{out} \tag{10}$$

$$PEC = \frac{j}{f} \tag{11}$$

$$j = \frac{\mathrm{Nu}}{\mathrm{Re}\cdot \mathrm{Pr}^{\frac{1}{3}}} \tag{12}$$

$$f = \frac{2de\Delta P}{v_{\text{in}}{}^{2}\rho L} \tag{13}$$

Where P_{in} (Pa) and P_{out} (Pa)represent the inlet and outlet pressures. Nu represents the Nusselt number, Re represents the Reynolds number, Pr represents the Prandtl constant.

Q (W)is the heat taken away by the coolant, as given by Eq. (14).

$$Q = c_p q_m \left(T_{out} - T_{in}\right) \tag{14}$$

Where q_m (kg·s^{-1}) is the mass flow rate at the inlet of the liquid cold plate, T_{in} (°C) and T_{out} (°C) are the inlet and outlet temperatures of the fluid.

2.5. Numerical Verification

To validate the numerical model, simulation results for lithium-ion battery thermal behavior were compared with experimental data from a $LiFePO_4$ battery [20]. The experiment measured the average temperature at five points on the battery during 1C and 2C discharge cycles. The simulation used the same parameters. As shown in Fig. 2(a), the deviation between the simulated and experimental maximum temperatures was less than 3% at both discharge rates, confirming the accuracy of the heat generation calculations and the model's reliability.

2.6. Grid independence verification

The computational mesh was generated using Fluent Meshing. The computational mesh was generated using Fluent Meshing with a Poly-Hexcore structure. To ensure numerical stability and accuracy, the mesh quality was strictly controlled: the maximum skewness was kept below 0.7, the

minimum orthogonal quality exceeded 0.3, and the maximum aspect ratio was maintained within 40. To accurately resolve the heat transfer at the fluid-solid interface, a three-layer prism boundary mesh was implemented with a first-layer height of 0.18 mm and a growth rate of 1.1. A mesh independence analysis was conducted to balance simulation accuracy and computational efficiency. Poly-Hexcore cells were used at a 2C discharge rate with a 0.04 kg/s mass flow rate. As depicted in Fig. 2(b), it was found that as the mesh count increased from approximately 2.2 million to 6.6 million, the average battery temperature decreased by about 5%. Further increases in mesh count resulted in only a minor temperature change of roughly 0.9%. Based on these results, a mesh count of 6,624,423 was selected as the optimal size for the numerical simulations. This process was repeated for each cold plate design to identify its specific optimal mesh size.

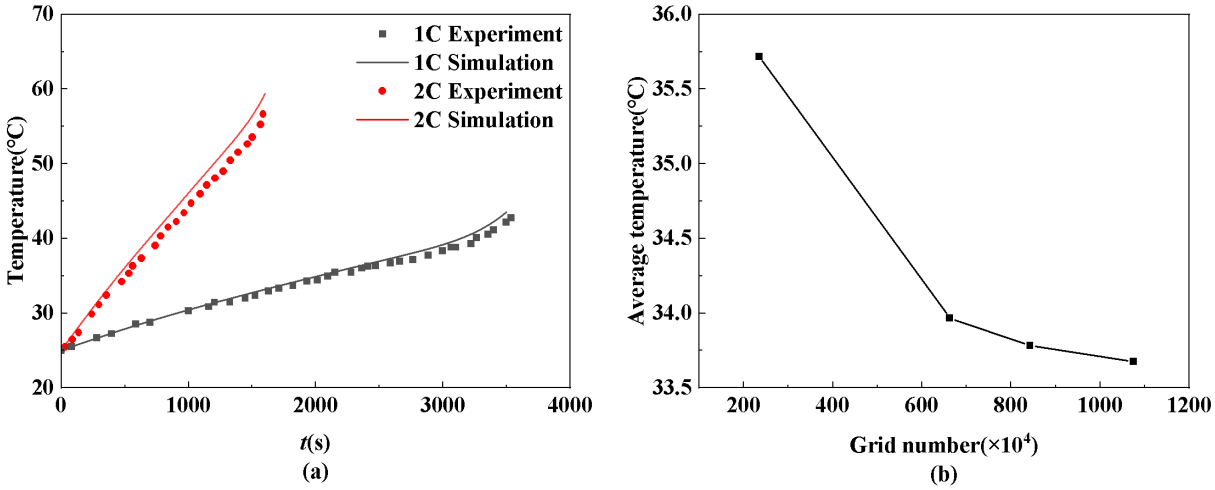

Fig. 2. (a) Changes in battery heating rate over time at different discharge rates.(b) Relationship between the average temperature of the battery and the number of grids.

3. Results and Discussion

3.1. Effect of liquid cooling plate structure

On the premise that the three flow channel structures have the same heat transfer area, a comparative analysis was conducted on the thermal management performance of fishbone, serpentine and parallel flow channels. By eliminating the influence of heat transfer area, the performance differences can more directly reflect the effects of geometric structure and flow organization.

As illustrated in Fig. 3, the fishbone flow channel exhibits the most superior performance in terms of cooling effect and temperature uniformity, with the maximum temperature T_{max} reaching only 37.33 °C and the temperature standard deviation T_{σ} dropping to as low as 0.55 °C. Regarding the liquid cooling plate performance, compared to the serpentine flow channel which generates an extremely high pressure drop $\triangle P$,exceeding 100,000 Pa, the fishbone flow channel maintains a significantly lower $\triangle P$ of only 4,929 Pa, effectively reducing the system's pumping power consumption. Furthermore, the comprehensive performance evaluation factor PEC results indicate that the fishbone structure 0.056 far outperforms the other two configurations. This fully demonstrates that the proposed optimization scheme achieves an excellent balance between heat transfer enhancement and energy consumption, showcasing its significant technical advantages.

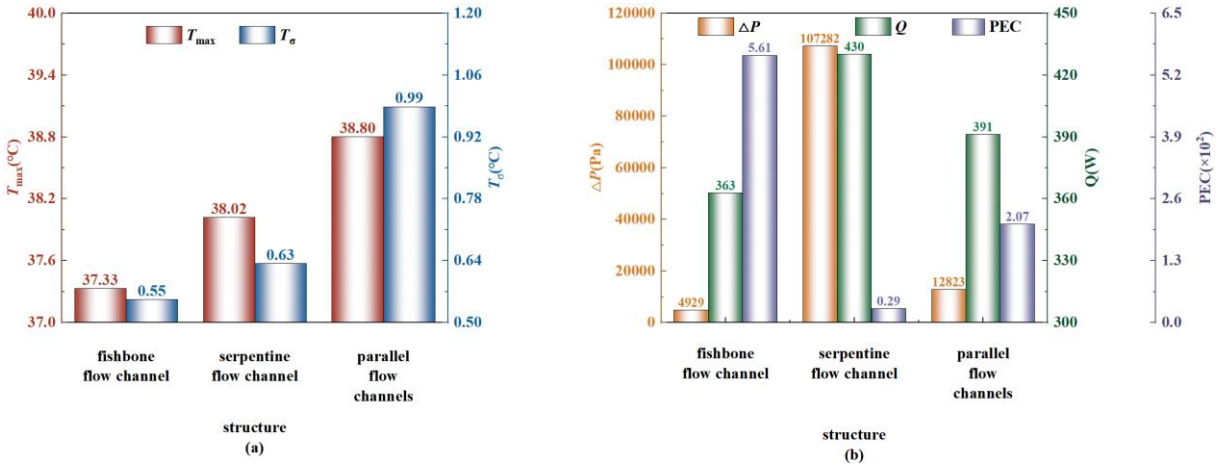

Fig. 3 Effect of iquid cooling plate on system performance. (a) battery pack T_{max} and T_σ. (b) liquid cooling plate$\triangle P$, Q and PEC.

3.2. Effect of main channel tapering

The tapered main channel's design strategy is to reduce its width along the flow direction gradually. The main channel width varies continuously, with the inlet fixed at 12mm. The outlet width is denoted as D. The baseline cold plate has a uniform main channel width of D=12mm, while other structures have outlet widths of D=6mm, D=4mm, and D=2mm, respectively.

As shown in Fig. 4(a), when the outlet width D is gradually decreased from 12 mm to 2 mm, the maximum battery temperature T_{max} initially decreases before slightly increasing. The observed values are 37.33 °C, 37.23 °C, 37.19 °C, and 37.21 °C, respectively, indicating reductions of approximately 0.10 °C, 0.14 °C, and 0.12 °C compared to the D=12 mm baseline. At D=2 mm, there is a slight increase, suggesting that moderate tapering can enhance heat transfer by increasing flow velocity. Excessive tapering may cause flow separation and localised heat buildup, restricting the cooling effect. The temperature standard deviation T_σ consistently decreases as D decreases, reaching 0.47 °C. At D=2 mm, there is a 0.04 °C decrease from D=12 mm, indicating better temperature uniformity. As shown in Fig. 3(b), the pressure drop ΔP and heat transfer capacity Q increase as D decreases. When D=2 mm, ΔP increases by 638.42 Pa compared to D=12mm, about 12%. Meanwhile, Q increases by 26.99 W, about 7%. The tapering barely affected the Performance Evaluation Criterion PEC, with a maximum increase of only 0.7% observed at a main channel outlet width of D = 2 mm.

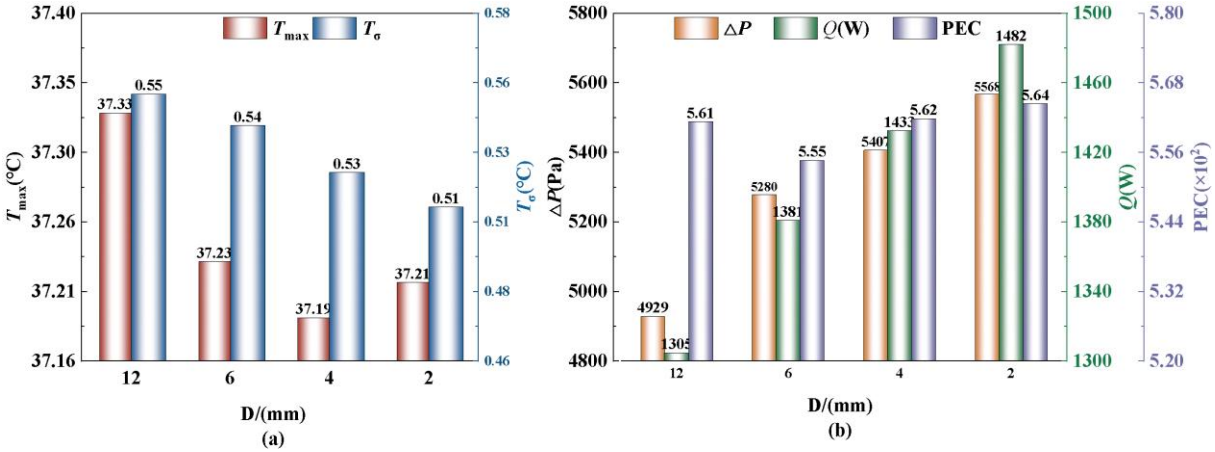

Fig. 4. Effect of D on system performance. (a) battery pack T_{max} and T_σ , (b) liquid cooling plate ΔP , Q and PEC.

Fig. 5 shows that as the cooling channel diameter D decreases, the high-temperature zone at the end of the battery pack shrinks, and the temperature distribution becomes more uniform. This occurs due to solid-solid conduction and solid-liquid convection between the batteries and the coolant, which continuously dissipates heat [22]. As shown in Fig. 6(a), a smaller D (4 mm and 2 mm) significantly lowers the coolant temperature at the channel's end, increasing the temperature difference with the battery surface and boosting heat transfer. Additionally, as illustrated in Fig. 6(b), a minor D raises the flow velocity in the downstream section of the main channel. According to the continuity equation, the reduced cross-sectional area velocity up the flow, thins the boundary layer, and enhances convective heat transfer between the channel wall and the adjacent battery surfaces. For a tapered main runner with D = 2 mm, the cooling fluid flow becomes more concentrated, leading to intensified heat exchange in localized regions. As a result, some areas of the battery are not sufficiently cooled, which in turn causes a higher maximum battery temperature [23].For D less than 6 mm, the heat transfer performance improvement outweighs the pressure drop increase, enhancing the PEC and slightly boosting overall performance.

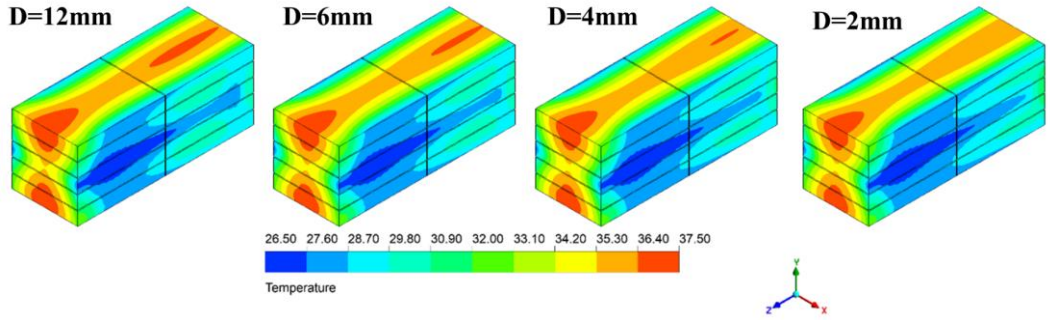

Fig. 5. Effect of D on battery pack temperature distribution.

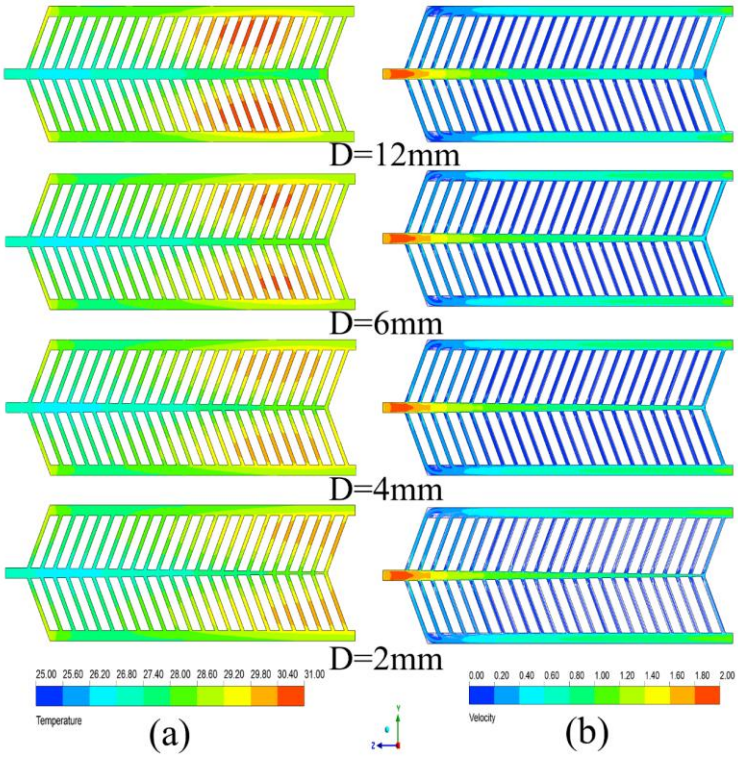

Fig. 6 Effect of D on the coolant: (a) Temperature and (b) Velocity distribution.

3.3. Effect of reducing the width of the rear branch flow channel

To improve heat transfer, this design reduces the width of the downstream branches while keeping the heat exchange area relatively constant. The main channel width is fixed at 12 mm, and the baseline branch width is 4 mm. For the optimized design, the width of the branches near the outlet is reduced, while the branches near the inlet remain 4 mm wide. The width of the branches near the outlet is denoted as W. Table 3 provides the detailed structural parameters.

Table3

Structural parameters for reducing the width of the rear branch of the fishbone flow channel.

Structural parameters	Mainchanne width (mm)	Number of branches	rear branch width (mm)	Area(mm^2)
W=4mm	12mm	48	4	0.0252
W=3mm	12mm	56	3	0.0252
W=2mm	12mm	72	2	0.0253
W=4-2mm	12mm	66	3.5,3,2.52	0.0257

As shown in Fig.7, performance changes are observed with a reduction in branch channel width. Compared to the W=4 mm configuration, the battery pack T_{max} does not change significantly. However, for both the W=2 mm and W=4-2 mm designs, T_σ decreases by 0.05 °C. The changes in ΔP and Q are also minimal. Additionally, the W=4-2 mm configuration, the Q and PEC decreased by 3% and 6%, respectively.

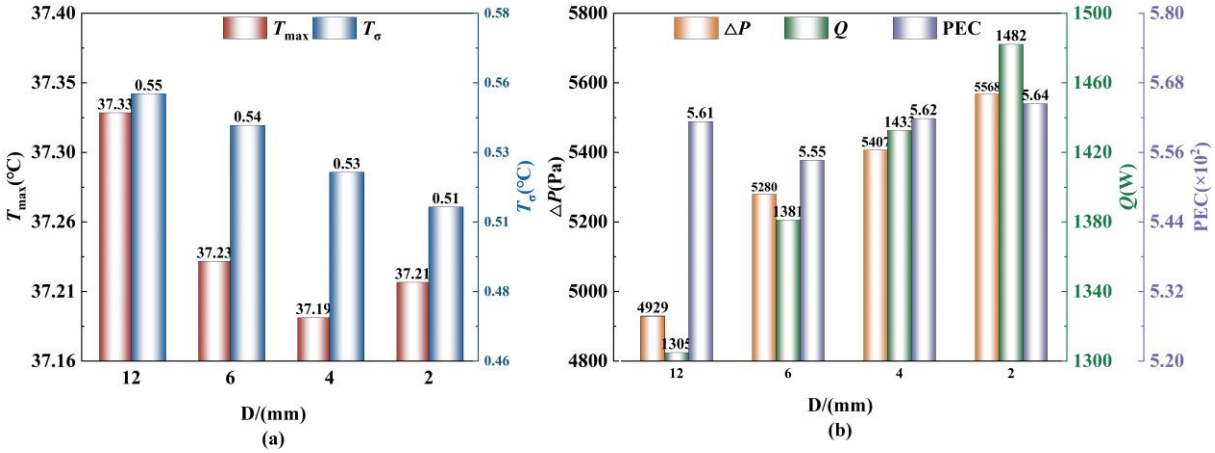

Fig. 7. Effect of W on system performance. (a) battery pack T_{max} and T_σ. (b) liquid cooling plate ΔP, Q and PEC.

As shown in Fig. 8, the W=2 mm and W=4-2 mm designs reduced the high-temperature regions at the end of the battery pack, indicating improved heat transfer performance in the downstream channels. Fig.9 further elucidate this phenomenon: while the overall high-temperature area of the coolant showed little change, the increased flow velocity in the downstream channels (particularly in the branches near the outlet) lowered the local coolant temperature. This enhanced local convective heat transfer and reduced the temperature gradient. However, these localized improvements contributed little to the overall system's heat exchange, so reducing the branch width had a minor impact on the total BTMS performance.

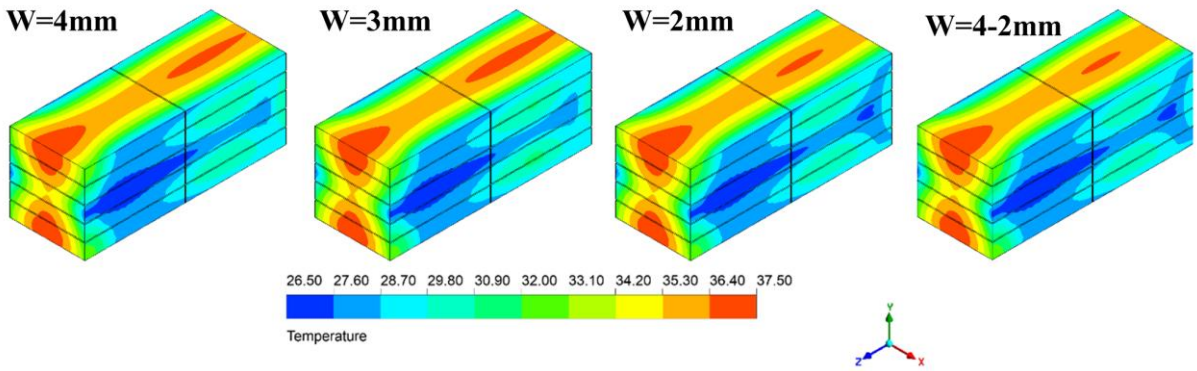

Fig. 8. Effect of W on battery pack temperature distribution.

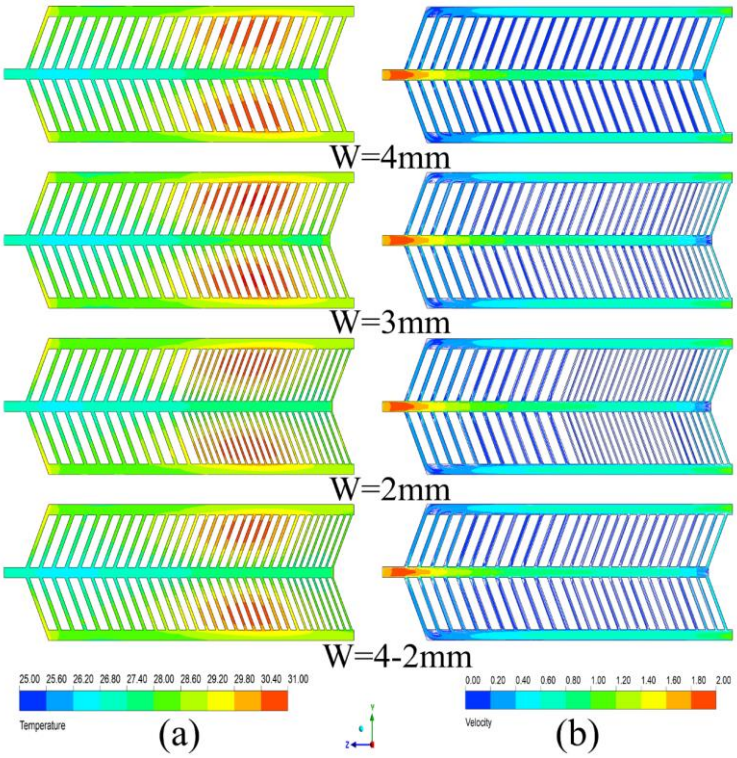

Fig. 9. Effect of width of W on the coolant: (a) Temperature and (b) Velocity distribution.

3.4. Effect of adding branch channels

Adding two branch channels at the inlet redirects some cold fluid to the downstream section. This effectively improves coolant distribution within the channels and further boosts the cooling performance. In this study, abbreviate the width of the added branch as L. Four branch widths were chosen: L=2 mm, L=4 mm, and L=6 mm, with L=0 mm representing the baseline liquid cold plate.

As depicted in Fig. 10, as L increases, $T_{\max}$ gradually decreases to 37.01 °C, 36.87 °C, and 36.79 °C, representing reductions of 0.32 °C, 0.46 °C, and 0.54 °C compared to the L=0 mm baseline. T_{σ} first increases and then decreases, with values of 0.53 °C and 0.52 °C at L=4 mm and L=6 mm, which are reductions of 0.02 °C and 0.03 °C, respectively. ΔP also decreases as L increases. The ΔP for the L=6 mm structure is 4064.77 Pa, a reduction of 864.57 Pa compared to the D=0 mm baseline, representing a decrease of approximately 18%. Conversely, both Q and PEC increase as L grows. At L=6 mm, Q and PEC are 372.04 W and 0.65, respectively. This shows an increase of 9.14 W and 0.0085 compared to

the D=0 mm baseline, representing approximately 3% and 15% increases. This indicates that adding diversion branches increases the heat transfer rate and significantly improves the heat transfer efficiency with the same pumping power.

As shown in Fig. 11 and Fig. 12(a), the high-temperature regions of the battery pack are significantly reduced as the branch width L increases. This effect works together with a more uniform coolant temperature distribution. Specifically, wider branches promote a more balanced coolant flow inside the battery pack, preventing localized overheating and enhancing heat removal. Fig. 12(b) shows that adding the branches decreases the flow velocity near the main channel. In contrast, the velocity inside the branches increases, leading to more uniform flow distribution within the channels. Although this adjustment partly weakens the convective heat transfer in specific areas, the added branches effectively expand the heat transfer area of the cold plate. At the same time, a reasonable flow velocity distribution improves coolant coverage. It increases residence time in heat-concentrated regions [24], enabling more complete heat exchange with the battery surface and effectively removing accumulated heat. Without branch channels, the coolant is concentrated in the main channel, forcing it to flow at a high velocity and causing a significant pressure drop due to increased frictional losses. As L increases from 4mm to 6mm, the flow distribution stabilizes, leading to minimal changes in coolant temperature and velocity and thus, no significant improvement in cooling.

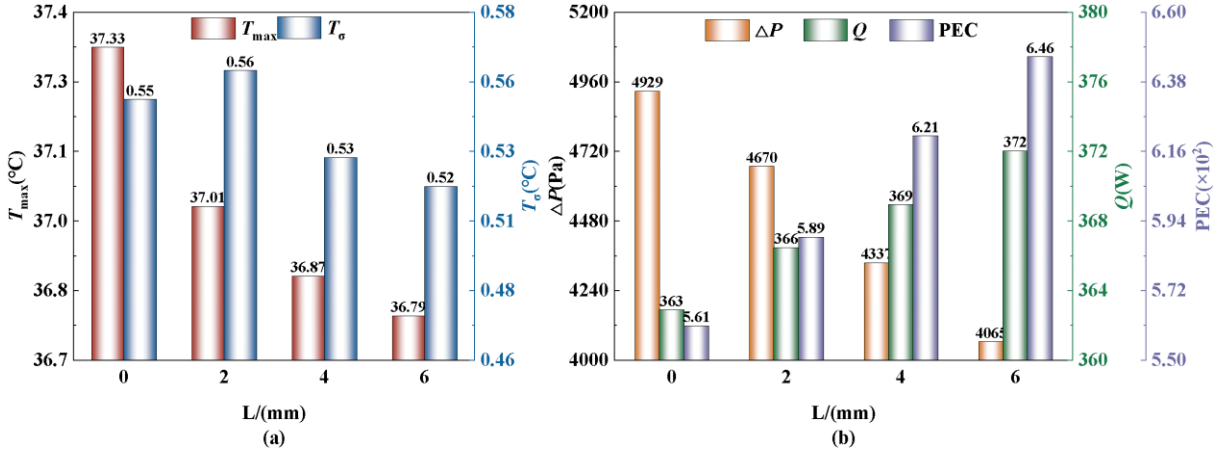

Fig. 10. Effect of L on system performance. (a) battery pack T_{max} and T_σ. (b) liquid cooling plate. ΔP, Q and PEC.

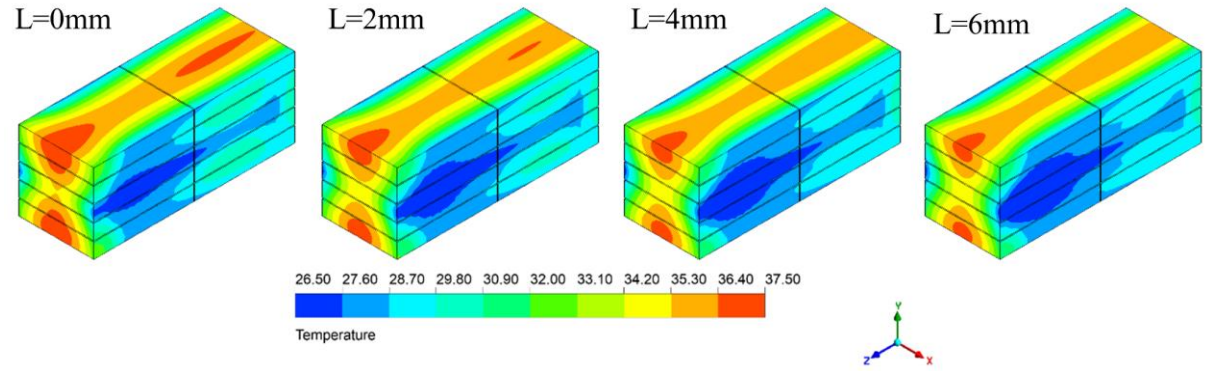

Fig. 11. Effect of L on battery pack temperature distribution.

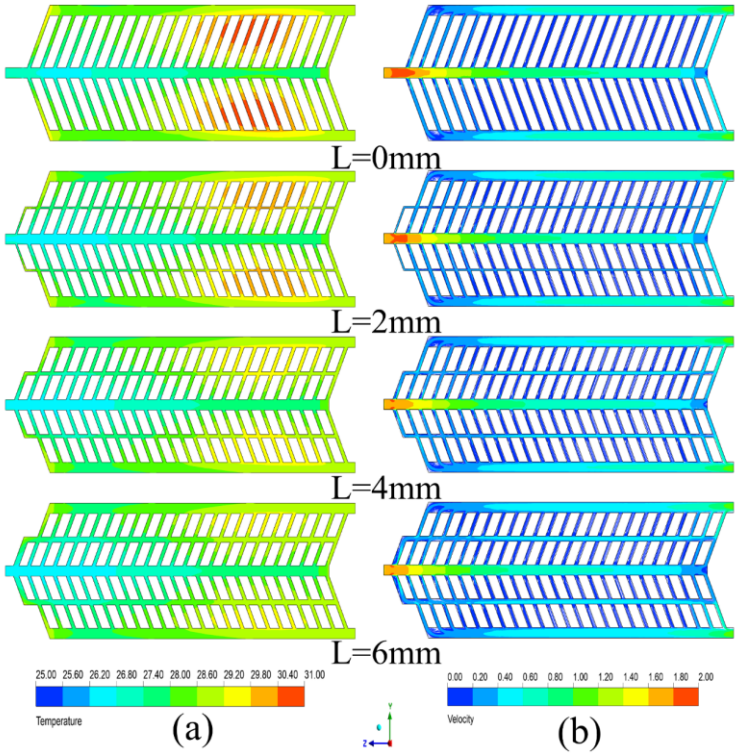

Fig. 12. Effect of L on the coolant: (a) Temperature and (b) Velocity distribution.

4. Conclusions

This study optimized the fishbone-shaped liquid cold plate through three strategies to enhance the thermal management of a battery pack. The main findings are summarized as follows:

(1) Tapering the main channel effectively reduces both $T_{\max}$ and T_{σ}. The lowest $T_{\max}$ of 37.19 °C is achieved at D=4mm, representing a reduction of 0.14 °C compared to the baseline. At D=2mm, T_{σ} reaches its minimum of 0.51°C, which is a decrease of 0.04 °C. However, ΔP increases by 12%. Although Q increases by 7%, the PEC only improves by 0.7%.

(2) Reducing the downstream branch width has no significant impact on $T_{\max}$, ΔP, or Q. In the W=4-2mm configuration, T_{σ} is 0.50 °C, which represents a reduction of 0.05 °C. However, this strategy leads to a 3% decrease in Q and a 6% decrease in the PEC, indicating a decline in overall efficiency.

(3) Adding branch channels is the most effective strategy for enhancing thermal performance while improving energy efficiency. As the branch length L increases, both $T_{\max}$ and T_{σ} continuously decrease. At L=6 mm, $T_{\max}$ is 36.79 °C, which is 0.54 °C lower than the baseline, and T_{σ} is 0.52 °C, showing an improvement of 0.03 °C. Simultaneously, ΔP is reduced by 17%, while Q and PEC increase by 3% and 15% respectively, demonstrating superior overall thermal management performance.

Acknowledgment

The authors gratefully acknowledge the financial support by Natural Science Fundamental Research Program of Shaanxi Province (Grant No. 2025JC-YBMS-558).

Nomenclature

C	discharge rate
c_p	specific heat[$J \cdot K^{-1}$]
D	outlet widths[mm]
d_e	hydraulic diameter
f	resistance coefficient
Q	the heat taken away by the coolant[W]
q_m	mass flow rate
Q_{gen}	heat generated during the battery charging
j	heat transfer coefficient
L	width of the added branch[mm]
Nu	Nusselt Number
PEC	comprehensive performance evaluation factor
h	heat transfer coefficient[$W \cdot m^{-2} \cdot K^{-1}$]
Re	Reynolds number
T	temperature[K]
T_{max}	maximum battery temperature[°C]
T_σ	standard temperature deviation[°C]
υ	velocity[m/s]
W	width of rear branch of the fishbone channel[mm]
ΔP	pressure drops [Pa]
Greek symbols	
ρ	density [$kg \cdot m^{-3}$]
λ	thermal conductivity[$W \cdot m^{-1} \cdot K^{-1}$]
μ	dynamic viscosity coefficient[$N \cdot s \cdot m^{-2}$]
Subscripts	
b	battery
in	inlet
max	maximum
out	outlet
Acronyms	
BTMS	battery thermal management system
EVs	electric vehicles
LIBs	lithium-ion batteries
PCM	phase change material
SOC	state of charge

References

[1] Xie, J., *et al*., Multi-level passive-active thermal control for battery thermal runaway prevention and suppression in electric vehicles, Etransportation, 26(2025), pp. 100467. DOI: 10.1016/J.ETRAN.2025.100467

[2] Sarvestani, A. B., *et al*., 3D numerical study of a novel fan-shaped heat sink with triangular cavities and nano-enhanced PCMs, *Applied Thermal Engineering*, 280(2025), p4, pp. 128408. DOI: 10.1016/J.APPLTHERMALENG.2025.128408

[3] Xiang, X., *et al*., Comparison between the cooling performances of micro-jet impingement systems using liquid metal and water as coolants for high power electronics, *International Journal of Thermal Sciences*, 173(2022), pp. 107375. DOI: 10.1016/J.IJTHERMALSCI.2021.107375

[4] Qi, W., *et al*., Multi-U-Style micro-channel in liquid cooling plate for thermal management of power batteries, *Applied Thermal Engineering*, 256(2024), pp. 123984. DOI: 10.1016/J.APPLTHERMALENG.2024.123984

[5] Fan, L., *et al*., Study on the cooling performance of a new secondary flow serpentine liquid cooling plate used for lithium battery thermal management, *International Journal of Heat and Mass Transfer*, 218(2024), pp. 124711. DOI: 10.1016/J.IJHEATMASSTRANSFER.2023.124711

[6] Aldawi F. Improving battery thermal management using superhydrophobic surfaces on mini-channel cold plates with zigzag and wavy walls. *Applied Thermal Engineering*, 276(2025), pp. 126953. DOI: 10.1016/J.APPLTHERMALENG.2025.126953

[7] Wu, J., *et al*., Investigation on enhancing thermal performance of the Li-ion battery pack with toothed liquid cooling plate and optimized flow channels, *Energy*, 315(2025), pp. 134343. DOI: 10.1016/J.ENERGY.2024.134343

[8] Gan, H., *et al*., Thermal performance of symmetrical double-spiral channel liquid cooling plate based battery thermal management for energy storage system, *Applied Thermal Engineering*, 263(2025), pp.125399. DOI: 10.1016/J.APPLTHERMALENG.2024.125399

[9] Xie, J., *et al*., A novel strategy to optimize the liquid cooling plates for battery thermal management by precisely tailoring the internal structure of the flow channels. *International Journal of Thermal Sciences*, 184(2023), pp. 107877. DOI: 10.1016/J.IJTHERMALSCI.2022.107877

[10] Zhu, J., *et al*. Numerical investigation and parameter optimization on a rib-grooved liquid-cooled plate for lithium battery thermal management system, *Journal of Energy Storage*, 85(2024), pp. 111085. DOI: 10.1016/J.EST.2024.111085

[11] Zhang, F., *et al*. Thermal performance analysis of a novel letter-type fin liquid cooling plate based on the field synergy principle and the second law of thermodynamics, *Thermal Science and Engineering Progress*, 56(2024), pp. 103027. DOI: 10.1016/J.TSEP.2024.103027

[12] Ahmed, H. E., Ahmed, M. I., Optimum thermal design of triangular, trapezoidal and rectangular grooved microchannel heat sinks, *International Communications in Heat and Mass Transfer*, 66(2015), pp.47-57. DOI: 10.1016/j.icheatmasstransfer.2015.05.009

[13] Mohapatra, J. R., *et al*., Indirect liquid-cooled lithium-ion battery module with improved circuitous minichannel cold plate design: a numerical study involving the effect of different flow

configurations, *Journal of Thermal Analysis and Calorimetry*, 150(2025), pp. 17841-17868. DOI: 10.1007/S10973-025-14647-1

[14] Fan, X., *et al*., Numerical optimization of the cooling effect of a bionic fishbone channel liquid cooling plate for a large prismatic lithium-ion battery pack with high discharge rate, *Journal of Energy Storage*, 72 (2023), Part A, pp. 108239. DOI: 10.1016/J.EST.2023.108239

[15] Yun, S., *et al*., Performance improvement of hot stamping die for patchwork blank using mixed cooling channel designs with straight and conformal channels, *Applied Thermal Engineering*, 165(2020), pp. 114562. DOI: 10.1016/j.applthermaleng.2019.114562

[16] Zhao, D., *et al*., Multi-objective optimization of battery thermal management system combining response surface analysis and NSGA-II algorithm. *Energy Conversion and Management*, 292(2023), pp. 117374. DOI: 10.1016/J.ENCONMAN.2023.117374

[17] Amalesh, T., Narasimhan, N. L., Introducing new designs of minichannel cold plates for the cooling of Lithium-ion batteries, *Journal of Power Sources*, 479(2020), pp. 228775. DOI: 10.1016/j.jpowsour.2020.228775

[18] Chen, K., *et al*., Optimization strategy for battery thermal management system with phase change materials, aerogel and cold plates, *International Journal of Heat and Mass Transfer*, 221(2024), pp. 125070. DOI: 10.1016/J.IJHEATMASSTRANSFER.2023.125070

[19] Yang, H., *et al*., A compact and lightweight hybrid liquid cooling system coupling with Z-type cold plates and PCM composite for battery thermal management, *Energy*, 263 (2023), Part E, pp. 126026. DOI: 10.1016/J.ENERGY.2022.126026

[20] Esmaeili, Z., Sheikholeslami, M., Enhanced thermal management of lithium-ion batteries using hybrid nanofluids in finned mini-channels: Energy and entropy analyses, *Engineering Science and Technology, an International Journal*, 66(2025), pp. 102069. DOI: 10.1016/J.JESTCH.2025.102069

[21] Yang, H., *et al*., Numerical study on cross-linked cold plate design for thermal management of high-power lithium-ion battery, *Batteries*, 9 (2023), 4, pp. 220. DOI: 10.3390/BATTERIES9040220

[22] Chen, F., *et al*., Topology optimization design and numerical analysis on cold plates for lithium-ion battery thermal management, *International Journal of Heat and Mass Transfer*, 183(2022), Part A, pp. 122087. DOI: 10.1016/J.IJHEATMASSTRANSFER.2021.122087

[23] Jiang, W., *et al*., Thermal performance enhancement and prediction of narrow liquid cooling channel for battery thermal management, *International Journal of Thermal Sciences*, 171(2022), pp. 107250. DOI: 10.1016/J.IJTHERMALSCI.2021.107250

[24] Xiao, G., *et al*., Battery performance optimization and multi-component transport enhancement of organic flow battery based on channel section reconstruction, *Energy*, 258(2022), pp. 124757. DOI: 10.1016/J.ENERGY.2022.124757

Received: 18.9.2025.
Revised: 12.3.2026.
Accepted: 25.3.2026.